Engineering Structures 262 (2022) 114308

Contents lists available at ScienceDirect

Engineering Structures

journal homepage: www.elsevier.com/locate/engstruct

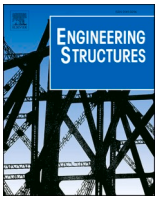

A novel crank inerter with simple realization: Constitutive model, experimental investigation and effectiveness assessment

Li Zhang [a,b], Songtao Xue [b,c], Ruifu Zhang [a,b,*], Linfei Hao [d], Chao Pan [e], Liyu Xie [b]

[a] State Key Laboratory of Disaster Reduction in Civil Engineering, Tongji University, Shanghai 200092, China
[b] Department of Disaster Mitigation for Structures, Tongji University, Shanghai 200092, China
[c] Department of Architecture, Tohoku Institute of Technology, Sendai 982-8577, Japan
[d] Guangdong Provincial Key Laboratory of Earthquake Engineering and Applied Technology, Guangzhou University, Guangzhou 510405, China
[e] College of Civil Engineering, Yantai University, Yantai 264005, China

ARTICLE INFO

Keywords:
Crank inerter
Apparent mass
Variable negative stiffness
Performance improvement

ABSTRACT

The inerter-based device is of increasing interest to scholars in the field of structural vibration control, which is characterized by apparent mass and negative stiffness effects. With this regard, it is potential to develop variable negative stiffness characteristics with the technology of inerter, which is promising to provide improved performance for structural vibration isolation and vibration suppression. In this study, the theoretical analysis and experimental investigation of a novel inerter element, named crank inerter, is performed. The presented crank inerter is proposed to generate a variable negative stiffness effect, which is realized on the basis of a crank mechanism. A constitutive model of crank inerter is developed to predict its mechanical behavior. For an in-depth understanding of the inertial property of the crank inerter, a parametric analysis is conducted on the inertia force calculation of the crank inerter. A prototype crank inerter is fabricated and tested under sinusoidal excitations to verify the proposed constitutive model. A variable negative stiffness of the crank inerter is reflected from the proposed constitutive model. The theoretical results calculated with the proposed constitutive model match well with the experimental data, which verifies that the proposed model can predict the mechanical behavior of the crank inerter. The dynamic analysis of a vibration isolator with a crank inerter is conducted to illustrate its effectiveness using the proposed constitutive model. The analysis results preliminarily show that the isolator with crank inerter can improve the structural performances regarding the peak force transmissibility and frequency band. Based on the presented investigations, a crank inerter with a simple configuration is summarized to be effective for providing an apparent mass effect and variable negative stiffness.

1. Introduction

During the past few years, the development of high-performance vibration control devices has increasingly attracted the interest of engineers and scholars to satisfy the performance demand of structures [1–5]. Recently, the inerter was introduced as a two-terminal inertia element to suppress unwanted structural vibrations, which are characterized by the apparent mass effect using a light gravitational mass [6–8]. The apparent mass effect of an inerter can be referred to as inertance, which is expressed as the ratio of the output force of the inerter to the relative acceleration of its two terminals. Apart from this, the negative stiffness effect is the other characteristic of inerter elements under dynamic excitations, which can be employed for improving structural vibration isolation and suppression [9,10]. Additionally, by employing the spring and damping elements together with inerter, the interaction between these elements can generate an enhanced damping effect compared to that of a single identical damping element [11,12]. This can provide better energy dissipation and be beneficial to structural vibration suppression. With the benefits mentioned above, inerter-based devices have been utilized as high-performance vibration control systems with different characteristics, e.g., tuned-type inerter systems with lightweight mass effects [13–18], performance-improved inerter-based vibration isolation systems [19–23], inerter-based high damping devices [6,24,25] and inerter-based devices with energy harvesting [26]. Scholars have proven these devices to be promising and efficient for structural vibration mitigation. The inerter-based devices are also

* Corresponding author.
E-mail address: zhangruifu@tongji.edu.cn (R. Zhang).

https://doi.org/10.1016/j.engstruct.2022.114308
Received 6 December 2021; Received in revised form 11 April 2022; Accepted 22 April 2022
Available online 6 May 2022

adopted in industrial and civil structures of China and Japan in practice [6,27].

The utilization of a two-terminal inertial element for structural vibration control dates back to the 1970 s in the field of civil engineering when Kawamata [28,29] proposed the mass pump as a passive control device by employing the gravity of fluid and a hydraulic mechanism between its two terminals. In the 2000 s, Saito et al. [30,31] and Ikago et al. [6,32] presented the ball screw mechanism to transform linear motion into a rapid rotation of a flywheel to fabricate an inerter device. They demonstrated the apparent mass effect and the efficient structural response mitigation effect of this inerter device through experimental tests. This device is also the inerter system adopted in practical building structures thus far. By utilizing the rack-and-pinion mechanism, the implementation of an inerter was proposed [7]. Using the flow of the liquid to drive the rotation of the hydraulic motor, Wang et al. [33] proposed a hydraulic inerter to generate the apparent mass effect. In addition, John and Wagg [34] presented a pivoted flywheel inerter using the living hinge mechanism and described the frictionless characteristic of this device. In summary, the implementation of an inerter generally involves the transformation of motion between two terminals of fluid-based devices or mechanical devices. For the studies illustrated above, all the inerters are characterized with constant inertance, and constant negative stiffnesses are provided by these inerters in a certain harmonic excitation. By utilizing the tuning or frequency adjustment function of these inerters in structures with a specified or predesigned parameter, the structural vibration can be suppressed in a limited frequency band.

For some structures, their loading conditions may be indefinite in the design phase or variable during the utilization stage, and their natural frequencies may vary due to damage or performance deterioration. Consequently, the devices with the aim of vibration control of such structures under external dynamic excitations are expected to behave improved performance, such as broadband characteristics, which can be addressed by additional devices with variable negative stiffness [35,36]. Considering that inerter devices are capable of generating negative stiffness effects, it can be attractive to develop variable negative stiffness characteristics by means of inerter. Combining the continuously variable transmission and rack-and-pinion mechanism, Lazarek et al. [37] proposed an adjustable inerter device, which can generate a variable negative stiffness effect. Faraj et al. [38] proposed a ball-screw inerter with a variable thread lead for the absorption of impact loadings. The variable negative stiffness is also generated by this inerter device. However, complex configurations are required for these two devices due to the employments of continuously variable transmission and ball-screw mechanisms. By putting inerter elements in geometrical nonlinear configurations, the geometrically nonlinear inerters that can generate variable negative stiffness effects are proposed by Moraes et al. [39] and Wang et al. [40]. However, these geometrically nonlinear inerters have only been studied from conceptual and theoretical perspectives, and there are no practical prototype devices for such geometrically nonlinear inerters. Hence, the development of a practical inerter device that generates variable negative stiffness with a simple realization can be helpful.

In this study, a novel crank inerter using the simple crank mechanism is proposed as an alternative inerter element to provide a variable negative stiffness, which is promising to improve the structural performance in vibration isolation and vibration suppression. The constitutive model is correspondingly derived to describe the mechanical behavior of the crank inerter. By the constitutive model, variable negative stiffness provided by the crank inerter is reflected. For an in-depth understanding of the inertial property, a parametric analysis is conducted further on the inertia force of the crank inerter. Then, a prototype crank inerter is designed and fabricated for experimental research. A series of dynamic tests on the crank inerter are conducted to verify the constitutive model, and the variable negative stiffness is correctly reflected by the proposed model. Dynamic analyses and comparative studies are also conducted for the vibration isolator with crank inerter to check its effectiveness.

2. Design and configuration of the crank inerter

Fig. 1 shows the implementation mechanism of the crank inerter element, where the simple crank mechanism is adopted to drive the flywheel to achieve the amplification of inertia. The crank inerter is mainly composed of three parts: a slider, a connecting rod and a flywheel. When the slider is moving in the linear direction under an external excitation, the sway of the connecting rod can drive the rotation of the flywheel, which can be seen as the key point for achieving the apparent mass effect characterized by the inerter. The relative displacement x between the two terminals of the crank inerter can be expressed as follows.

$$x_1 - x_2 = x \tag{1}$$

where x_1 and x_2 are the right and left absolute displacements of the two terminals of the crank inerter. In Fig. 1, the distance between points O and B in the crank inerter is denoted asx_B. l and r represent the length of rod AB and crank OA, respectively, and R is the radius of the flywheel. The angle between OA and OB is denoted asφ, while β denotes the angle between OB and AB.

Based on the implementation mechanism presented above, in this study, the configuration of a crank inerter device is proposed considering its application in practice, as shown in Fig. 2. Flywheels are symmetrically arranged in the crank inerter taking into account their stability. Unlike the implementation mechanism plotted in Fig. 1, the linear motion of the slider is replaced by the linear motion of a rod in the crank inerter, which is constrained by the linear motion guide attached on the support frame. Additionally, the crank inerter in Fig. 2 is designed to facilitate its replaceability in applications for the utilization of the flange connection and fabricated support frame. The proposed crank inerter is expected to provide an effective and simple inerter element with apparent mass and variable negative stiffness characteristics. From the perspective of the physical implementation of crank inerter illustrated above, its variable negative stiffness is generated by the nonlinear relationship between the linear motion of the slider and the rotation of the flywheel. The variable negative stiffness of the crank inerter will be proven and illustrated in detail in Section 3.

3. Constitutive model formulation

3.1. Derivations

As illustrated above, the crank inerter proposed in this study involves translational motion of the linear motion rod, sway of the connecting rod and rotation of the crank with its attached flywheels. To derive the corresponding constitutive model, the geometrical relations, kinematic relations and force transformations in a crank inerter are analyzed below. These analyses are conducted primarily to obtain the mathematical relationship between the linear and rotational motions and the mechanical relationship between the internal force and its corresponding motion in a crank inerter, which is considered the crucial part for the derivation of a constitutive model of a typical inerter. Note that the

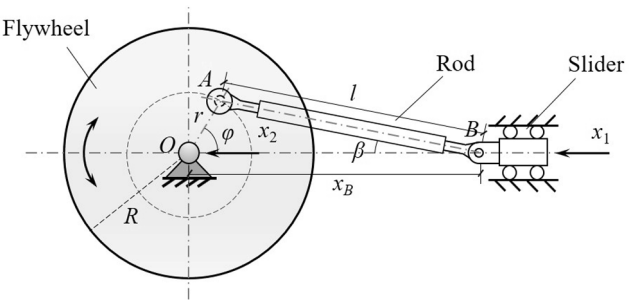

Fig. 1. Schematic representation of crank inerter.

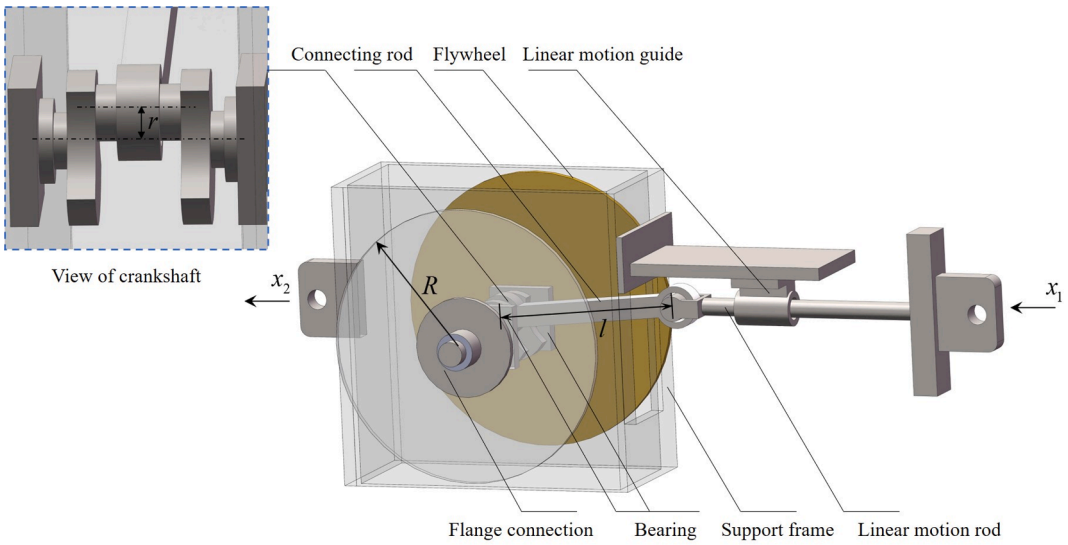

Fig. 2. Configuration of a crank inerter device.

derivations below are based on the assumption of a rigid crank inerter. To keep the rationality of this assumption, the stiffnesses of components in the crank inerter should be designed large enough to avoid non-negligible deformations. The generation of friction heating in the crank inerter also needs to be kept in a lower grade.

Geometrical relations. The significant geometrical relations in a crank inerter are first described herein. As shown in Fig. 1, the distance x_B can be calculated as.

$$x_B = r\cos\varphi + l\cos\beta \tag{2}$$

There is a constrained condition in the crank mechanism expressed as.

$$r\sin\varphi = l\sin\beta \tag{3}$$

According to the cosine theorem, $\cos\varphi$ can be calculated in $\triangle$AOB as follows:

$$\cos\varphi = \frac{x_B^2 + r^2 - l^2}{2x_B \cdot r} \tag{4}$$

Note that for a crank inerter, the value of x_B ranges from $l-r$ to$l+r$. During the working stage of a crank inerter, the motion of the linear motion rod is recommended to be less than its boundary value. Hence, the value of angle φ can be considered in the range of zero toπ. $\sin\varphi$ can be expressed as.

$$\sin\varphi = \left(1-\cos^2\varphi\right)^{\frac{1}{2}} = \frac{\left[2l^2\left(r^2+x_B^2\right) - \left(r^2-x_B^2\right)^2 - l^4\right]^{\frac{1}{2}}}{2x_B \cdot r} \tag{5}$$

Kinematic relations. A kinematic analysis is conducted to illustrate the kinematic relations in a crank inerter. For the crank inerter, the left direction of x is considered positive in this study. Given an initial distance of points O and B denoted asx_{B0}, the distance $x_B(t)$ with respect to time t can be expressed as.

$$x_B(t) = x_{B0} - x(t) \tag{6}$$

where $x(t)$ is the relative displacement of the crank inerter with respect to$t$. According to Eq. (6), the relationships between the derivates of x_B and x with respect to t can be written as.

$$\dot{x}_B(t) = -\dot{x}(t), \ddot{x}_B(t) = -\ddot{x}(t) \tag{7}$$

where $\dot{x}_B(t)$ and $\ddot{x}_B(t)$ are the first and second derivates of distance x_B with respect to$t$, respectively; $\dot{x}(t)$ and $\ddot{x}(t)$ are the first and second derivates of displacement x with respect to$t$, respectively.

Taking the first and second derivates of both φ and x_B with respect to t at both ends of Eq. (4), the angular velocity $\dot{\varphi}$ and angular acceleration $\ddot{\varphi}$ of the flywheel can be calculated as.

$$\dot{\varphi} = \frac{r^2 - x_B^2 - l^2}{2rx_B^2\sin\varphi}\dot{x}_B \tag{8}$$

$$\ddot{\varphi} = \frac{1}{\sin\varphi}\cdot\left[\frac{2\left(l^2-r^2\right)\cdot\dot{x}_B^2 + \left(r^2-l^2-x_B^2\right)x_B\cdot\ddot{x}_B}{2rx_B^3} - \dot{\varphi}^2\cos\varphi\right] \tag{9}$$

Force transformation. To obtain the constitutive equation of the crank inerter, the transfer of forces in the crank inerter under external excitation F is subsequently depicted as shown in Fig. 3. The transfer process of forces in the crank inerter can be described as follows: the total reaction force F can be divided into the summation of the friction force F_f and the force F_l of the crank inerter along the linear motion rod to be transferred to the connecting rod, by assuming that the reciprocating inertia force of the linear motion rod is ignored due to its small mass compared to the flywheel; the force F_l can be divided into the lateral pression F_c of the guide and the force F_l along the connecting rod; and F_l can be further divided into the radial force F_n and the tangential forceF_t. Consequently, F_t drives the rotation of the flywheel in the crank inerter. Although the friction force F_f is only marked on the interface of the slider in Fig. 3, the total friction effect of the crank inerter (e.g., the friction effect generated at points A and B) is included in F_f for simplification.

Through the division of forceF_l, the forces F_c and F_l can be calculated according to the parallelogram rule of force as follows:

$$F_c = F_l\tan\beta \tag{10}$$

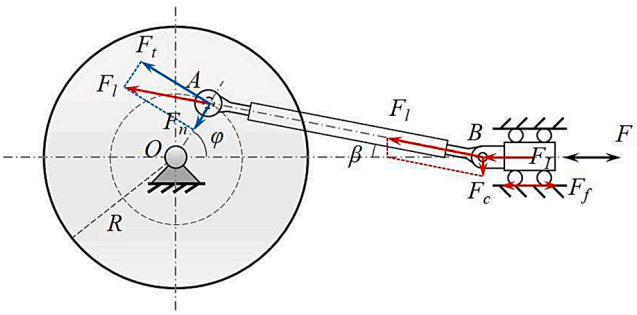

Fig. 3. Relationships between forces in the crank inerter.

$$F_l = F_I/\cos\beta \tag{11}$$

The forces F_n and F_t can be obtained by dividing the forceF_l, expressed as.

$$F_n = F_I\cos(\varphi+\beta)/\cos\beta \tag{12}$$

$$F_t = F_I\sin(\varphi+\beta)/\cos\beta \tag{13}$$

The flywheel in the crank inerter is directly driven by the forceF_t. According to the moment equilibrium principle of the flywheel with respect to point O, F_t satisfies the expression as follows:

$$I_m\ddot{\varphi} = F_t r = F_I r\sin(\varphi+\beta)/\cos\beta \tag{14}$$

where $I_m = m_0R^2/2$ is the moment of inertia of the circular flywheel with massm_0. Rewriting Eq. (14), the force F_I can be expressed as.

$$F_I = \frac{I_m\ddot{\varphi}\cdot\cos\beta}{r\sin(\varphi+\beta)} \tag{15}$$

According to the derivation above, the force F_I is eventually balanced against the rotational inertia of the flywheel through the force transformation in the crank inerter. Hence, the force F_I is considered the inertia output force of the crank inerter. Substituting Eqs. (2)-(9) into Eq. (15), for a crank inerter with a certain size and specifiedx_{B0}, the inertia output force F_I can be rewritten as follows:

$$F_I = I_m[a(x)\ddot{x} + b(x)\dot{x}^2] = f_{I1} + f_{I2} \tag{16}$$

where $a(x)$ and $b(x)$ can be expressed as.

$$a(x) = \frac{\left[(x_{B0}-x)^2 + l^2 - r^2\right]^2}{(x_{B0}-x)^2\left\{2l^2\left[r^2+(x_{B0}-x)^2\right] - \left[r^2-(x_{B0}-x)^2\right]^2 - l^4\right\}} \tag{17}$$

$$b(x) = \frac{\left[r^2-l^2-(x_{B0}-x)^2\right]\left[\left(l^2-r^2\right)^3 + \left(3r^4+2l^2r^2-5l^4\right)(x_{B0}-x)^2 + 3\left(l^2-r^2\right)(x_{B0}-x)^4 + (x_{B0}-x)^6\right]}{(x_{B0}-x)^3\left\{2l^2\left[r^2+(x_{B0}-x)^2\right] - \left[r^2-(x_{B0}-x)^2\right]^2 - l^4\right\}^2} \tag{18}$$

$f_{I1} = I_m a(x)\ddot{x}$ is part of the inertia output force related to displacement x and acceleration$\ddot{x}$, and $f_{I2} = I_m b(x)\dot{x}^2$ is part of the inertia output force related to displacement x and velocity$\dot{x}$. These two expressions are performed to provide better insight into the analysis of inertia output forceF_I. The term f_{I1} in the expression of the inertia force of the crank inerter is similar to the reaction force of a typical inerter, even though it also depends on the terminal displacement x of the crank inerter. Although f_{I2} has a damping-like expression, it actually results from the inertia effect of the crank inerter and arises due to the relationship between the terminal displacement x and rotation of the flywheel in the crank inerter. This can be seen and understood from the above derivation and the working mechanism of the crank inerter. These two terms are further investigated through a parametric analysis for an in-depth understanding of the inertial property of the crank inerter in Subsection 3.2.

The inertia force F_I of the crank inerter is also checked from an energy perspective. Assuming the terminal displacement x is harmonic, i.e.,$x = Xe^{iwt}$, the corresponding velocity and acceleration can be expressed as $\dot{x} = (Xw)ie^{iwt}$ and$\ddot{x} = -Xw^2e^{iwt}$, respectively, where X is the amplitude of the terminal motion of the crank inerter, i is the imaginary unit and w denotes the circular frequency of the external excitation. In one vibration cycle, the work of F_I in the crank inerter is calculated as.

$$W_I = \int_0^{\frac{2\pi}{w}} F_I\dot{x}dt = \int_0^{\frac{2\pi}{w}} f_{I1}\dot{x}dt + \int_0^{\frac{2\pi}{w}} f_{I2}\dot{x}dt \tag{19}$$

Substituting Eqs. (16)-(18) and the harmonic terminal motion of the crank inerter into Eq. (19) gives.

$$\int_0^{\frac{2\pi}{w}} f_{I1}\dot{x}dt = 0, \int_0^{\frac{2\pi}{w}} f_{I2}\dot{x}dt = 0, W_I = \int_0^{\frac{2\pi}{w}} f_{I1}\dot{x}dt + \int_0^{\frac{2\pi}{w}} f_{I2}\dot{x}dt = 0 \tag{20}$$

which indicates that there is no energy dissipation in the crank inerter in one vibration cycle. The forcesF_I, f_{I1} and f_{I2} are all conservative forces.

In addition, according to Eq. (16), the value of the inertia output force F_I of the crank inerter relies on the displacement$x$, velocity $\dot{x}$ and acceleration $\ddot{x}$ of the linear motion rod. This is quite different from the typical linear inerter device, whose inertia output force is proportional to the terminal acceleration. Under the assumption of harmonic terminal motion of the crank inerter, the relationship between the displacement$x$, velocity $\dot{x}$ and acceleration $\ddot{x}$ can be expressed as$\dot{x}^2 = (x - X^2/x)\ddot{x}$. Substituting this equation into Eq. (16), the inertia output force F_I of the crank inerter can be rewritten as.

$$F_I = I_m[a(x)\ddot{x} + b(x)\dot{x}^2] = \frac{m_0R^2}{2}\left[a(x) + b(x)\cdot\left(x - \frac{X^2}{x}\right)\right]\left(\ddot{x}_1 - \ddot{x}_2\right) \tag{21}$$

Then, the inertance m_{in} of the crank inerter can be expressed as.

$$m_{in} = \frac{F_I}{\ddot{x}_1 - \ddot{x}_2} = \frac{m_0R^2}{2}\left[a(x) + b(x)\cdot\left(x - \frac{X^2}{x}\right)\right] \tag{22}$$

The apparent mass effect of crank inerter can be reflected by Eq. (22). In addition, according to Eq. (22), the value of m_{in} is related to the terminal displacement x and the corresponding amplitude X of the crank inerter. Hence, unlike the typical inerter device, the inertance m_{in} of the crank inerter is considered not constant but variable. Further, the negative stiffness k_{in} of the crank inerter is also considered variable, which is graphically illustrated by the inertial behavior of crank inerter below (Fig. 4). The negative stiffness k_{in} can be expressed as.

$$k_{in} = \frac{F_I}{x_1 - x_2} = -w^2\frac{m_0R^2}{2}\left[a(x) + b(x)\left(x - \frac{X^2}{x}\right)\right] \tag{23}$$

From the perspective of the physical implementation and theoretical analysis of crank inerter above, its variable negative stiffness is generated by the nonlinear relationship between the linear motion of the slider and the rotation of the flywheel.

Generally, friction in a mechanical device is inevitable. To derive the constitutive equation, the friction force existing in the crank inerter is considered. Coulomb friction is assumed to model the friction effect, and the friction force F_f can be calculated as.

$$F_f = f_c sgn(\dot{x}) \tag{24}$$

$$sgn(\dot{x}) = \begin{cases} 1, \dot{x} > 0 \\ 0, \dot{x} = 0 \\ -1, \dot{x} < 0 \end{cases} \tag{25}$$

where f_c is the magnitude of the Coulomb friction force.

By adding the inertia and friction effect together, the constitutive equation of the crank inerter can be expressed as follows:

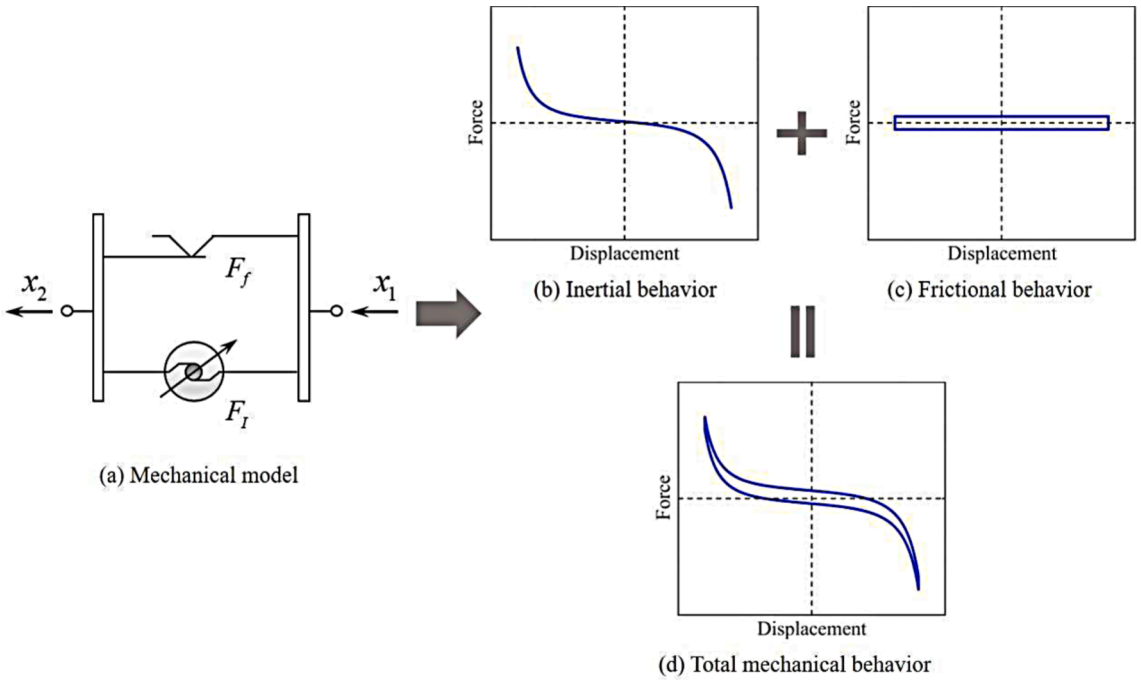

Fig. 4. Mechanical model and behaviors of a crank inerter.

$$F = F_I + F_f = I_m[a(x)\ddot{x} + b(x)\dot{x}^2] + f_c sgn(\dot{x}) \tag{26}$$

As a consequence, the mechanical behavior of the crank inerter can be represented by an inerter element with variable inertance and a friction element connected in parallel. Fig. 4 shows the corresponding mechanical model and the schematic force–displacement loops of the crank inerter. The energy dissipation effect is not exhibited by the force–displacement loop of the inertial behavior in the crank inerter (Fig. 4b). The slope of the curve in Fig. 4b is negative and continuously variable, which is different from the constant slope of the inertial force–displacement loop of a typical inerter. The constant negative slope is described as the negative stiffness effect of a typical inerter. Hence, it can be said that a crank inerter can behave a continuously variable negative stiffness effect. Fig. 4c shows the hysteretic curve of the Coulomb friction presented with a rectangular curve, and the superposition of the inertial and frictional behaviors composes the total mechanical behavior of the crank inerter shown in Fig. 4d. Note that these schematic force–displacement loops are qualitatively presented and obtained based on the derivations above using a certain harmonic excitation.

3.2. Parametric analysis of inertia force

The inertial behavior of a crank inerter is addressed in this section. To present the characteristics of the two terms, f_{I1} and f_{I2}, in the calculation of the inertia force of the crank inerter, a parametric analysis is conducted herein. Given $r = 15mm$, $R = 130mm$, $x_{B0} = l = 100mm$ and $m_0 = 10kg$ in a crank inerter, the values of f_{I1} and f_{I2} are calculated using Eq. (16) and shown in Fig. 5. When x is relatively small (approximately $-r/3 \leqslant x \leqslant r/3$), the value of f_{I1} is largely independent of the change in displacement x and proportional to acceleration $\ddot{x}$, as shown in Fig. 5a. This means that the force f_{I1} can be considered linear with a small x, which is the same as a typical linear inerter. For a large x, the value of f_{I1} depends both on x and $\ddot{x}$ and is nonlinear. In Fig. 5b, for a relatively small displacement x ($-r/3 \leqslant x \leqslant r/3$), the value of f_{I2} is approximately a

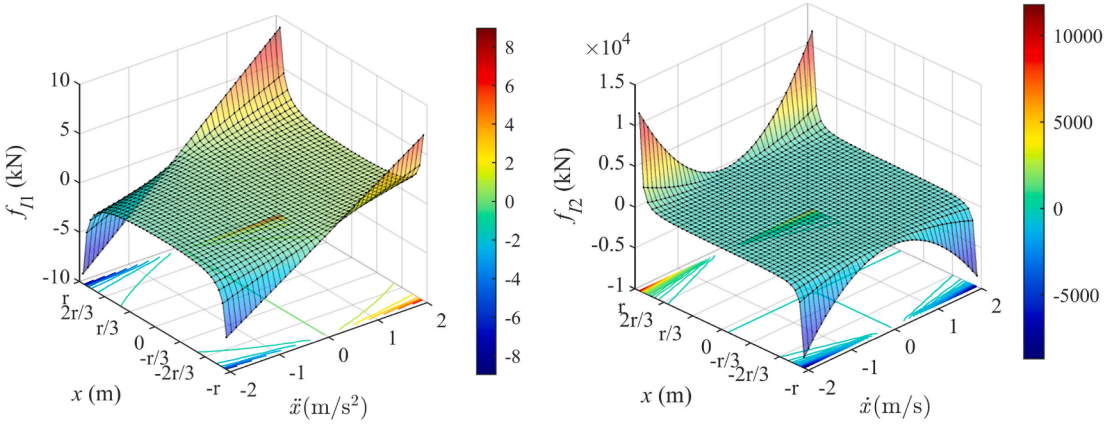

(a) f_I (b) f_{I2}

Fig. 5. Inertia forces of the crank inerter.

horizontal plane close to the plane of$f_{I2} = 0$, which means that the force f_{I2} related to x and $\dot{x}$ can be ignored for calculation of the inertia force of the crank inerter when x is small. Accordingly, for a large$x$, f_{I2} is obviously nonlinear with the change of x and$\dot{x}$.

The stroke of a crank inerter is correlated with the initial position of the linear motion rod measured byx_{B0}. To ensure that the crank inerter can be reciprocally driven with an equal stroke r in both the positive and negative directions, the value of x_{B0} is recommended to be equal to l for the application of the crank inerter, which is also adopted in the parametric analysis above. Based on this condition, the crank inerter can be concluded to provide an approximate linear inertia force when x is small ($-r/3 \leqslant x \leqslant r/3$) and a nonlinear inertia force when x is large, according to the numerical analysis above. Since the upper limit for the stroke of a crank inerter depends on the value of$r$, which is related to the inertial output force of the crank inerter, the trade-off between the stroke and inertial output force should be considered for the design of a crank inerter. An additional displacement-restricted friction mechanism can also be beneficial to update the crank inerter device considering safety reasons.

4. Experimental testing

4.1. Testing setup and specimen detail

To obtain the mechanical behavior and verify the derived constitutive model, a prototype device is fabricated based on the proposed configuration of a crank inerter for experimental investigation, as shown in Fig. 6. The total length and stroke of the crank inerter are 450 mm and $\pm$ 15 mm, respectively. Considering the limitation of the installation space of the testing rig shown in Fig. 6, flywheels of the crank inerter are placed in the horizontal direction rather than vertical direction, which is different from the schematic configuration of the crank inerter shown in Fig. 2. Note that the direction of flywheels has no impact on the mechanical behavior of the crank inerter. The specifications of the crank inerter are listed in Table 1. A hydraulic servo actuator with a built-in displacement sensor is used for the dynamic test of the crank inerter. A load cell placed between the actuator and crank inerter is adopted to measure the reacting force of the crank inerter, as shown in Fig. 6. The output force, frequency range and working stroke of the actuator are 0–15 kN, 0–10 Hz and $\pm$ 100 mm, respectively. Two accelerometers are placed at one of the ends of the crank inerter, and the other end of the crank inerter is fixed on the testing rig. Sinusoidal excitations with different amplitudes and frequencies are employed to conduct the dynamic test, which are generated with the displacement control mode.

Table 1
Specifications of crank inerter.

Parameter of CI	Value
Total length of crank inerter (mm)	450
Stroke (mm)	$\pm$ 15
Elastic modulus of material E (MPa)	200 GPa
Length of connecting rod l (mm)	100
Diameter of connecting rod d_1 (mm)	20
Diameter of linear motion rod d_2 (mm)	15
Length of crank r (mm)	15
Radius of flywheel R (mm)	130
Radius of flange R_1 (mm)	40
Mass of flywheel m_0 (kg)	1.787, 3.624, 7.812
Mass of flange m_1 (kg)	0.427

4.2. Test cases

Based on the theoretical analysis of the mechanical behavior of the crank inerter, its inertance is considered variable in general. In particular, the inertance of the crank inerter can be considered to be approximately constant under a small displacement amplitude excitation($-r/3 \leqslant X \leqslant r/3$). Hence, the reaction forces of the crank inerter are experimentally checked under sinusoidal excitations with both large and small displacement amplitudes. The presented constitutive model of the crank inerter is verified with the experimental results for different test cases. For the crank inerter with a flywheel of 1.787 kg, dynamic tests are conducted under 2 Hz sinusoidal excitations with variable amplitudes of 11 mm, 12 mm and 13 mm, which are seen as test cases with large displacement amplitudes. In particular, under sinusoidal excitation with a frequency of 2 Hz and amplitude of 12 mm, dynamic tests are also conducted for a crank inerter with flywheel weights of 3.624 kg and 7.812 kg to comprehensively present the mechanical behavior of the crank inerter. The flywheel of the prototype device used for testing is designed to be easily replaced using the flange connection. Sinusoidal excitation with a 5 mm amplitude is considered the small displacement amplitude excitation for these experiments. For the crank inerter with a flywheel of 7.812 kg, dynamic tests are conducted using 5 mm sinusoidal excitations with frequencies of 0.5 Hz, 1 Hz, 1.5 Hz, 2 Hz and 3 Hz. Note that in all of the crank inerter test cases, the initial distances x_{B0} before loading are designed to be equal to$l$.

5. Results and discussions

The reaction forces of the crank inerter are presented in this section for the different test cases illustrated above. The experimental measurements of the crank inerter are mainly characterized by two groups of excitations, large and small displacement amplitudes, based on the theoretical analyses in Section 3. The proposed constitutive model of

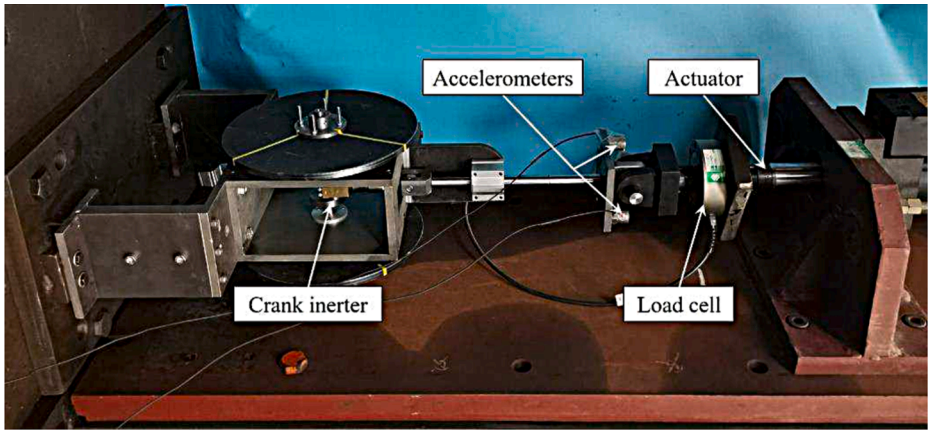

Fig. 6. Photograph of the experimental setup for the dynamic test of the crank inerter.

crank inerter is verified through comparisons between the theoretical results and the experimental test data.

5.1. Inertia forces of the crank inerter under large displacement amplitude excitations

5.1.1. Experimental results

Comparisons between the experimental output forces and calculated forces, including the total reaction force and inertia output force, are conducted here to verify the proposed constitutive equation of a crank inerter under large displacement amplitude excitations. According to the experimental test data, the estimated value of Coulomb friction for the proposed constitutive model of the prototype crank inerter is identified using the nonlinear least squares method. The theoretical inertia forces are calculated using Eq. (16) based on the testing displacement and acceleration. The total reaction forces of the crank inerter are obtained with Eq. (26).

For the crank inerter with a flywheel mass of 1.787 kg, the experimental result, total reaction force and inertia force are shown in Fig. 7 under sinusoidal excitation with a frequency of 2 Hz and amplitude of 12 mm. The theoretical reaction forces agree well with the experimental results in the time history expression and hysteretic loops, which verifies the proposed calculation of the constitutive model of the crank inerter. Under an observation of the blue line in Fig. 7b, a variable negative stiffness effect is shown by the force–displacement loop of the inertia force of the crank inerter, and the tangent stiffness in this curve increases with the increase in displacement of the crank inerter. In addition, no energy dissipation effect is shown in the force–displacement loop of inertia force, whereas slight energy dissipation behavior in the force–displacement loop of the experimental result for the crank inerter is shown with the black dotted line in Fig. 7b. This can be attributed to the friction force in the crank inerter. Fig. 7c exhibits the force-acceleration loop of the crank inerter. An obvious nonlinear relationship between the inertia force and relative acceleration can also be observed for the crank inerter, and the increasing rate of inertia force evidently increases with increasing acceleration. According to the definition of inertance(inertia force/relative acceleration), the inertance of the crank inerter is considered variable and nonlinear.

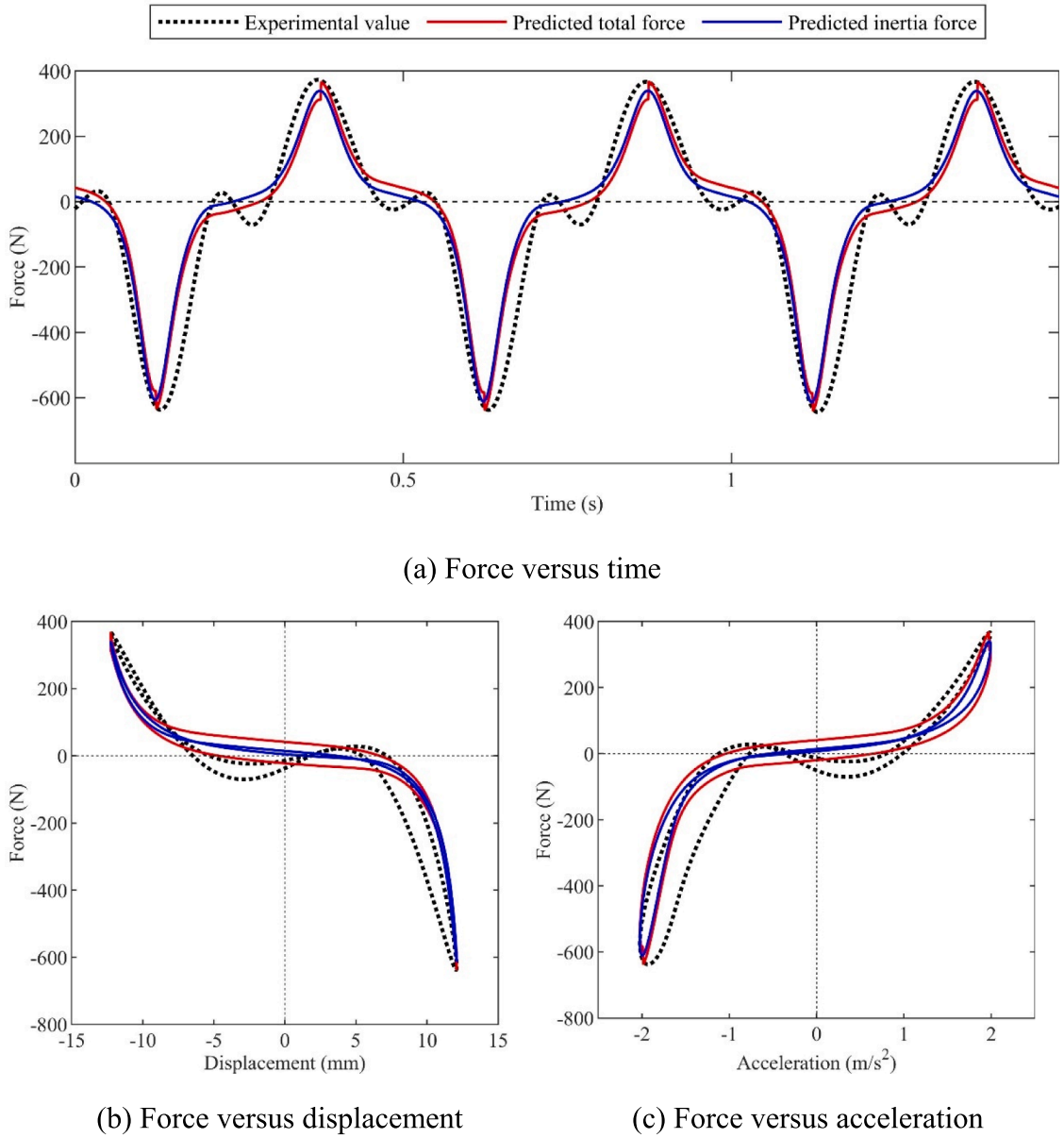

(a) Force versus time

(b) Force versus displacement

(c) Force versus acceleration

Fig. 7. Experimental and theoretical forces of the crank inerter under large displacement amplitude sinusoidal excitation (frequency: 2 Hz, amplitude: 12 mm).

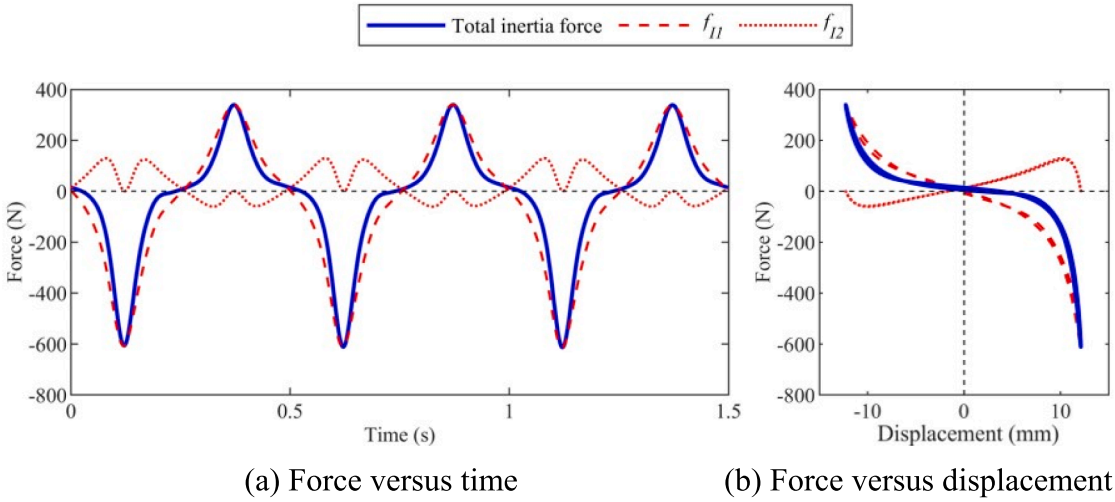

Fig. 8. Composition of the inertia force in the crank inerter (frequency: 2 Hz, amplitude: 12 mm).

Although the initial distance x_{B0} is set to be equal to $l = 100$ mm before loading, the actual x_{B0} may not be exactly equal to 100 mm in the experiment under a manually operated initial position of the actuator. In this test case, the actual x_{B0} is identified as 99.5 mm using the nonlinear least square method. This parameter is mainly related to the absolute value of the maximum and minimum reaction forces of the crank inerter. In addition, because the original moment of inertia $I_{m,0}$ of the crank inerter is difficult to calculate considering the irregular shape and mass distribution of the crankshaft, this parameter also needed to be measured experimentally and was determined to be $1.72 \times 10^4 kg{\cdot}mm^2$ in this test case.

In this study, the expression of the inertia force of the crank inerter is divided into two terms, expressed as f_{I1} andf_{I2}. For the test case above, the total inertia force of the crank inerter calculated using Eq. (16) and its components, f_{I1} andf_{I2}, are presented in Fig. 8 to display the contributions of these two components to the total result. The values of f_{I1} are close to the total inertia force of the crank inerter, especially for their maximum and minimum values. A relatively large value of f_{I2} is obtained when the terminal displacement is close to its amplitude. The term f_{I1} can be seen as the main contributor to the total inertia force of the crank inerter, but the impact of the value of f_{I2} on the total inertia force cannot be ignored. As shown in Fig. 8b, neither of the force–displacement loops of inertia force, f_{I1} andf_{I2}, exhibit the energy dissipation effect, which is consistent with the theoretical analysis of Eq. (20).

The force–displacement loops of the crank inerter with $m_0 = 1.787kg$ are compared under sinusoidal excitations with a certain frequency of 2 Hz and amplitudes of $X = 11$ mm, $X = 12$ mm and $X = 13$ mm to comprehensively exhibit the inertia force and total reaction force of the crank inerter, as shown in Fig. 9. Good agreement can be observed between the experimental and theoretical reaction forces for different excitation amplitudes. A more evident nonlinear behavior of the inertia force of the crank inerter is shown for a larger amplitude excitation, which indicates a lager negative stiffness for a larger excitation amplitude. Furthermore, it is observed that the maximum inertia force of the crank inerter increases rapidly with increasing excitation amplitude under a certain frequency excitation. When the excitation amplitude increases from 11 mm to 13 mm (i.e., an increase of the amplitude of 2 mm) for the frequency of 2 Hz, the maximum inertia force of the crank inerter increases by more than one time. Using Eqs. (22) and (23), the inertances and negative stiffnesses of the crank inerter at the maximum displacement amplitudes are calculated, respectively, as listed in

Table 2
Values of m_{in} and k_{in} of crank inerter at different maximum amplitudes.

	Maximum amplitude of the excitation		
	$X = 11mm$	$X = 12mm$	$X = 13mm$
Inertance m_{in} (kg)	199.8	356.9	409.8
Negative stiffness k_{in} (N/mm)	−31.6	−56.4	−64.7

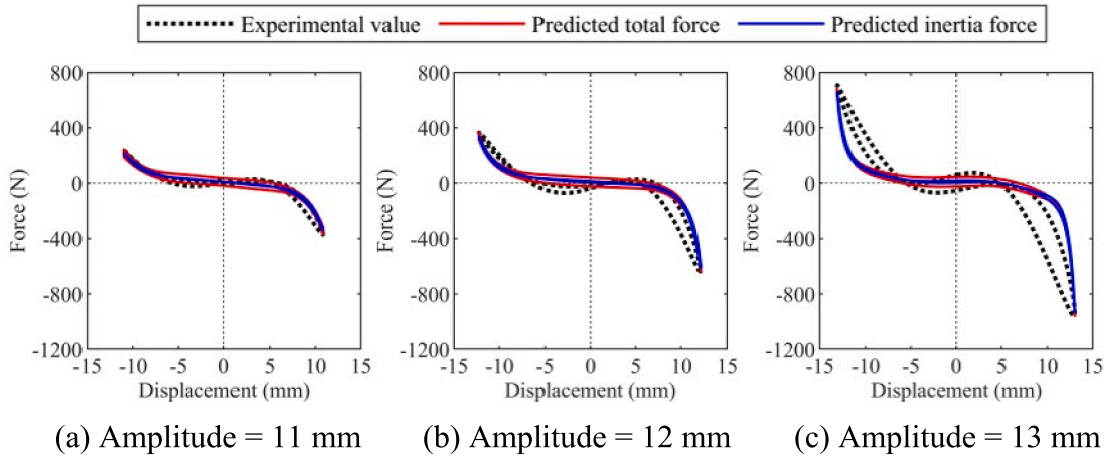

Fig. 9. Force-displacement loops of the crank inerter under 2 Hz sinusoidal excitations with different amplitudes ($m_0 = 1.787kg$).

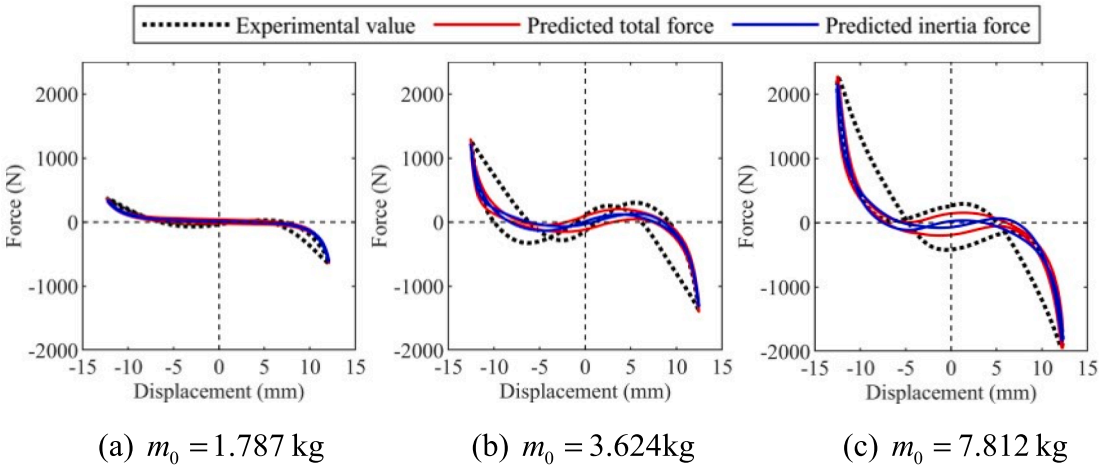

Fig. 10. Force-displacement loops of crank inerter with different flywheel masses (frequency = 2 Hz, amplitude = 12 mm).

Table 2. A rapid increase in the inertance and negative stiffness at the maximum displacement amplitude for the crank inerter are obtained with the increase in excitation amplitude. Hence, a large inertia force is produced by the additional crank inerter in structures when there is a large displacement response, which usually occurs during severe vibration of structures. Additionally, for these three test cases, all the actual initial distances x_{B0} are identified as 99.5 mm because the actuator can automatically return to the same initial location after a test case.

Fig. 10 compares the force–displacement loops of the crank inerter with different flywheel masses under a certain sinusoidal excitation with a frequency of 2 Hz and amplitude of 12 mm. The tendency of the theoretical value matches well with the experimental inertia force of the crank inerter for different flywheel masses. Furthermore, the maximum output inertia forces of the crank inerter with different flywheels are approximately proportional to the weight of the flywheel. Different characteristics of the relationships between the absolute values of maximum and minimum forces are observed for the test cases with different flywheel weights. For the test case of $m_0 = 1.787kg$, the absolute value of the maximum force is evidently less than that of the minimum force. However, for$m_0 = 3.624kg$, these two absolute values are approximately equal, and for$m_0 = 7.812kg$, the absolute value of the maximum force is larger than that of the minimum force. This phenomenon is mainly caused by the different values of x_{B0} in these test cases. Due to the replacement of the flywheel in the experimental test, the initial distance x_{B0} needs to be manually reset for each case. Hence, different values of x_{B0} may occur around the expected value of 100 mm for x_{B0} in these test cases. The actual values of x_{B0} for the cases of $m_0 = 1.787kg$, $m_0 = 3.624kg$ and $m_0 = 7.812kg$ were determined to be 99.5 mm, 100.1 mm and 100.3 mm, respectively.

5.1.2. Discussions

It is shown in Fig. 10(b) and 10(c) that the positive slopes occurred near zero displacements of the crank inerter. This phenomenon may be raised by the unsmooth rod due to the degradation of components in the crank inerter. The backlash is another reason for the positive slopes, which can cause the lag of force when the direction of the displacement is changed in the crank inerter [41,42]. In addition, discrepancies between the theoretical and experimental results are shown in force–displacement loops above for the crank inerter, especially for the testing cases with large reaction forces. One of the reasons for the discrepancy is the backlash existed in the prototype crank inerter due to the mechanical manufacture, which is not considered in the proposed constitutive model. By updating the mechanical manufacturing techniques, the backlash in crank inerter can be significantly reduced. Readers of interest of the backlash in an inerter device can refer to the research by Wang and Su [42]. The other reason for the discrepancy between experimental and theoretical results is due to gradual degradation of the components of crank inerter during the testing. This is also indicated by relatively large discrepancies in the testing cases with large reaction forces. The degradation of the components of crank inerter can cause different friction coefficient during a testing case, which differs from the adopted ideal Coulomb friction mode. However, this model is still recommended due to its simplicity and acceptable accuracy. The gradual degradation of the components of crank inerter cause different friction forces for different testing cases. As a consequence, the friction forces for the cases of$m_0 = 1.787kg$, $m_0 = 3.624kg$ and $m_0 = 7.812kg$ are identified as 24.2 N, 54.1 N, and 67.3 N, respectively.

Noted that the cross phenomenon for backward and forward parts occurs in force–displacement loops above, which is considered unreasonable according to the derived constitutive model of the crank inerter. This phenomenon occurred in experimental curves is mainly caused by the existence of backlash in prototype crank inerter, which can also be found in the experimental study of the inerter device by Nakamura et al [25]. The cross phenomenon in blue force–displacement loops of theoretical output inertia forces is considered due to degradation of components in crank inerter, which is more obvious in later testing cases and testing cases with lager output inertia forces.

5.2. Inertia forces of the crank inerter under large displacement amplitude excitations

According to the parametric analysis results in Section 3.2, the inertance of a crank inerter can be approximately constant under a small displacement amplitude excitation (approximately $-r/3 \leqslant X \leqslant r/3$). In this study, an excitation amplitude of 5 mm is set as a small displacement for the prototype crank inerter. Dynamic tests are conducted for a crank inerter with a flywheel weight of 7.812 kg to check its mechanical performance under 5 mm sinusoidal excitations with frequencies of 0.5 Hz, 1 Hz, 1.5 Hz, 2 Hz and 3 Hz.

Fig. 11 shows the experimental result, total reaction force and inertia force of the crank inerter under sinusoidal excitation with a frequency of 2 Hz and amplitude of 5 mm. The theoretical value obtained with Eq. (26) matches the experimental result under a small displacement excitation. The experimental result (Fig. 11b) of the crank inerter exhibits an obvious enclosed area in the force–displacement loop. This is because the backlash in the inerter device and actuator may be comparable to the small displacement amplitude. Additionally, test cases of small displacement excitation are conducted after all of the large displacement excitations. Hence, the degradation of the components in the crank inerter can also be an influencing factor. For the force–displacement loop of inertia force of the crank inerter, the enclosed area is much

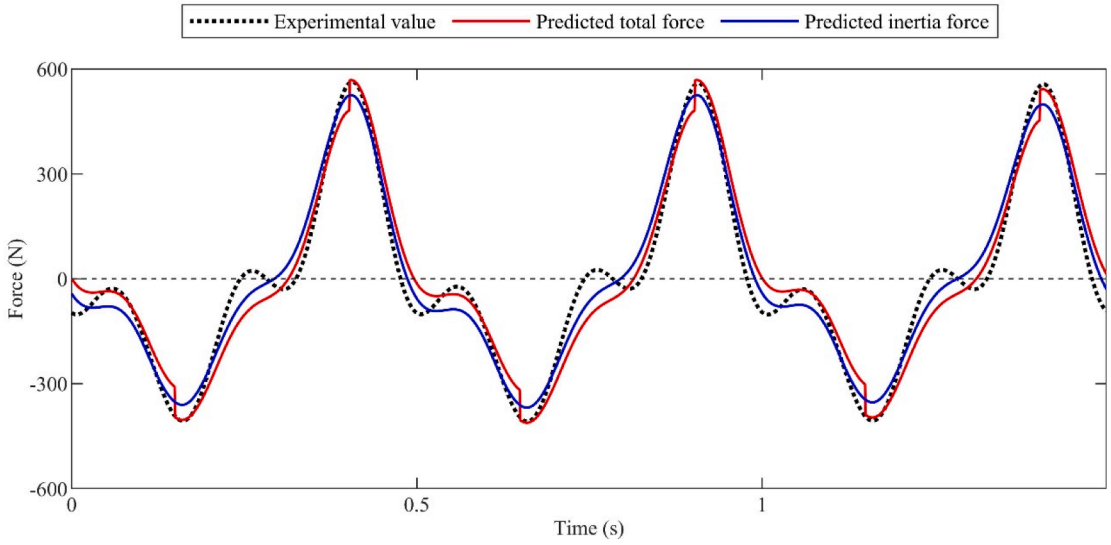

(a) Force versus time

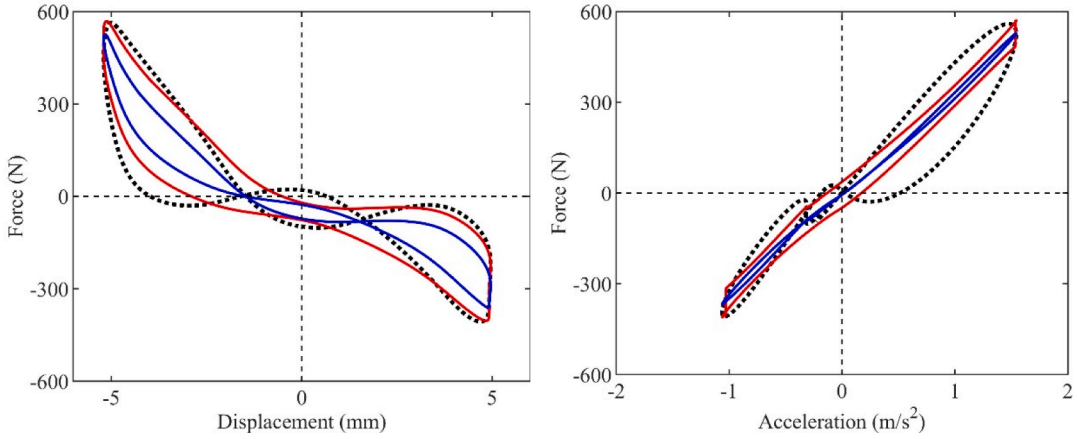

(b) Force versus displacement (c) Force versus acceleration

Fig. 11. Experimental and theoretical inertia forces of the crank inerter under small displacement amplitude sinusoidal excitation (frequency: 2 Hz, amplitude: 12 mm).

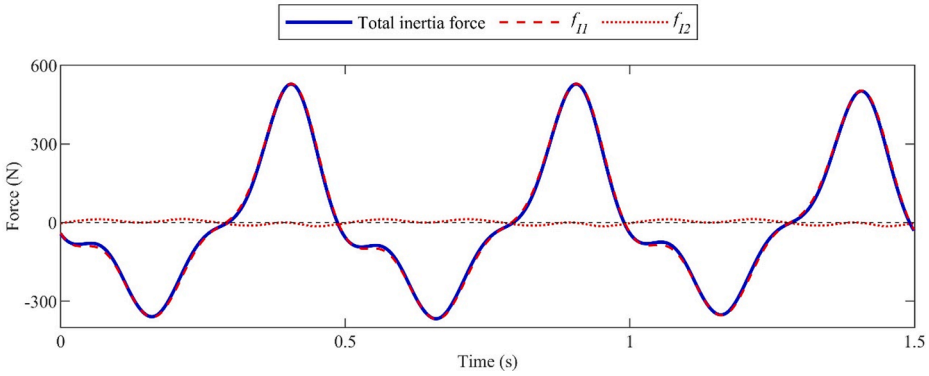

Fig. 12. Composition of the inertia force in crank inerter (frequency: 2 Hz, amplitude: 12 mm).

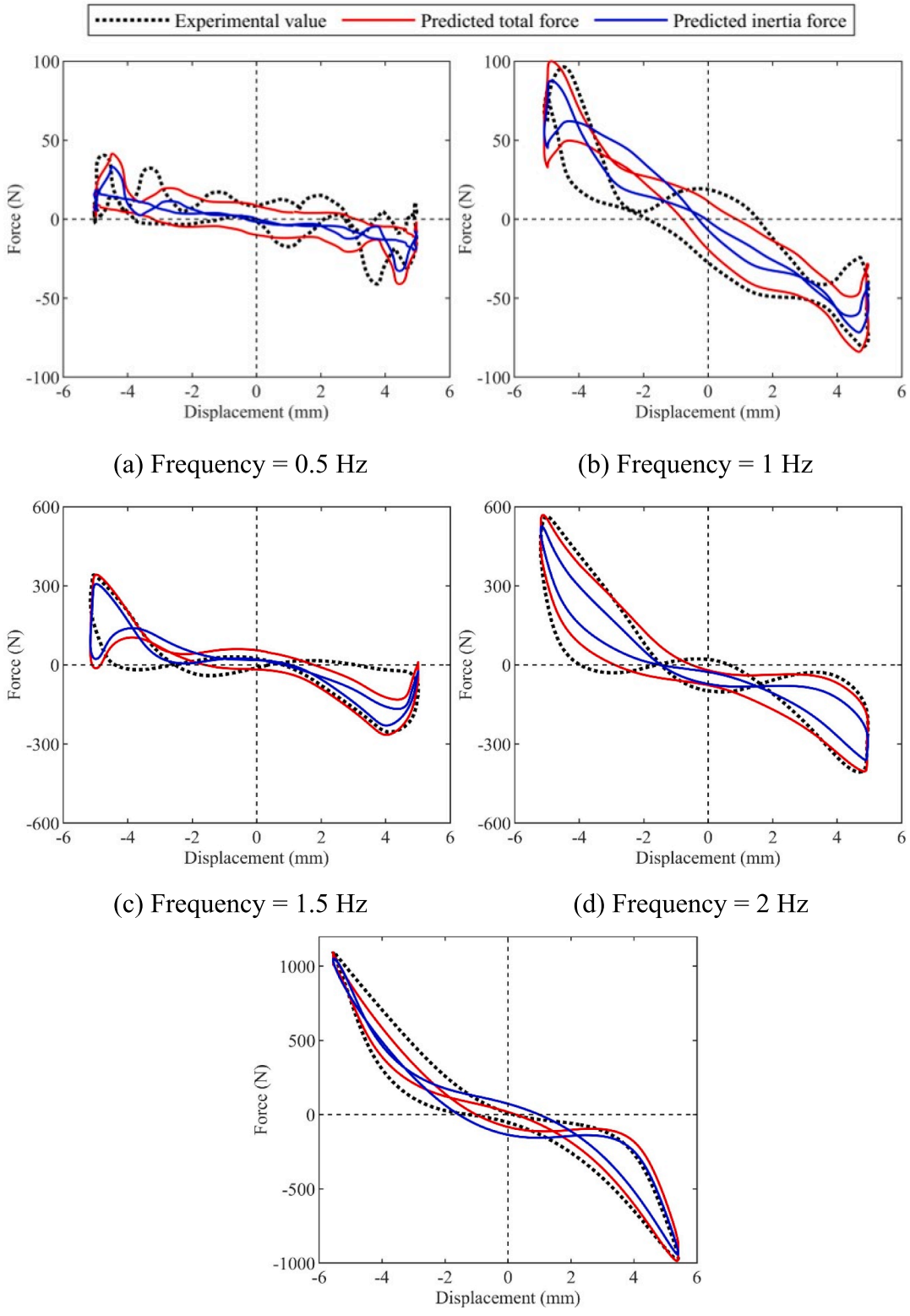

Fig. 13. Force-displacement loops of the crank inerter under 5 mm sinusoidal excitations with different frequencies ($m_0 = 1.787kg$).

smaller. An approximately linear tendency between the inertia force and displacement is shown for the force–displacement loop, which indicates an approximate constant negative stiffness is provided by crank inerter under a certain small displacement amplitude excitation. Fig. 11c shows the corresponding force-acceleration loop. The inertia force of the crank inerter is almost proportional to the acceleration. Hence, the inertance of the crank inerter can be considered constant under a small displacement amplitude excitation, which verifies the parametric analysis result above.

According to the Eq., the calculation of inertia force is divided into two terms, f_{I1} andf_{I2}. These two terms and the total inertia force are exhibited in Fig. 12 to check their contribution to the total inertia force. The values of f_{I1} are almost equal to the total inertia force of the crank inerter, whereas the values of f_{I2} are close to zero. This indicates that the inertia force related to the terminal velocity of the crank inerter can be ignored under a small displacement amplitude excitation, which is consistent with the parametric analysis in Section 3.2.

Fig. 13 shows the force–displacement loops of the crank inerter under 5 mm sinusoidal excitations with frequencies of 0.5 Hz, 1 Hz, 1.5 Hz, 2 Hz and 3 Hz. The calculated reaction forces using Eq. (26) matches the experimental results for all test cases with different excitation frequencies. Under small displacement excitations, the relationship between the inertia force and displacement is approximately linear for different excitation frequencies. An approximately constant negative stiffness effect for the crank inerter is shown by the force–displacement loops of inertia forces in Fig. 13 under a certain small displacement amplitude excitation. With increasing excitation frequency, the negative stiffness of the crank inerter increases under 5 mm sinusoidal excitations.

6. Example

To check the effectiveness of the proposed crank inerter for structural vibration suppression, this device is adopted in a vibration isolator and its performances are compared with the uncontrolled vibration isolator, and the vibration isolator equipped with classic inerter whose negative stiffness and inertance is constant under a certain harmonic excitation. The mechanical model of a vibration isolator with crank inerter is shown in Fig. 14, where$m$,c, and k are the isolated mass, stiffness and damping coefficient of the isolator, respectively, f_e and ω are the amplitude and frequency of the harmonic force excitation, respectively. Note that, for simplification, the friction action of crank inerter is ignored in the dynamic analysis of the corresponding isolator below, considering that the friction force of this device is slight according to the experimental and theoretical results above. This is a common manipulation for the dynamic analysis of the structure with inerter devices.

By employing the expression of the inertial force F_I in Eq. (16), the equation of motion for the vibration isolator with crank inerter can be written as follows:

$$\left(m+\frac{m_0R^2}{2}a(y)\right)\ddot{y}+\frac{m_0R^2}{2}\cdot b(y)\dot{y}^2+c\dot{y}+ky=f_e\cos\omega t \tag{27}$$

where$y$, $\dot{y}$ and $\ddot{y}$ denote the displacement, velocity and acceleration of the mass relative to the base with respect to the time$t$, respectively, $a(y)$ and $b(y)$ can be calculated using Eq. (17) and (18), respectively. For convenience, the following non-dimensional parameters are defined as.

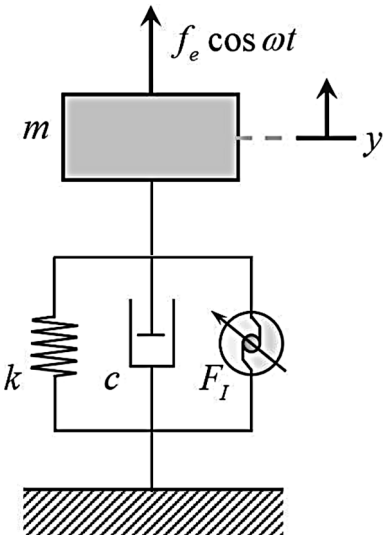

Fig. 14. Diagram of a vibration isolator with crank inerter.

$$\mu=\frac{m_0}{m},\xi=\frac{c}{2\sqrt{mk}},\omega_0=\sqrt{\frac{k}{m}},\gamma=\frac{R}{r}$$
$$Y=\frac{y}{r},\tau=\omega_0 t,\Omega=\frac{\omega}{\omega_0},F_e=\frac{f_e}{kr} \tag{28}$$

where μ is mass ratio of the flywheel of crank inerter to the isolated object, ξ and ω_0 are the damping ratio and frequency of the isolator without crank inerter, respectively, γ denotes the ratio of the radius of the flywheel to that of the crank, and$Y$,τ, Ω and F_e are the non-dimensional displacement, the non-dimensional time, the non-dimensional excitation frequency and force amplitude, respectively.

Using the non-dimensional parameters above, Eq. (27) can be rewritten in a dimensionless form as follows:

$$\left(1+\frac{\mu\gamma^2}{2}A(Y)\right)Y'+\frac{\mu\gamma^2}{2}B(Y)^2+2\xi Y'+Y=F_e\cos(\Omega\tau) \tag{29}$$

where the primes are differentiation with respect toτ, $A(Y)$ and $B(Y)$ are the non-dimensional expressions of $a(y)$ and$b(y)$, respectively, given as.

$$A(Y)=\frac{\left[(X_{B0}-Y)^2+L^2-1\right]^2}{(X_{B0}-Y)^2\left\{2L^2\cdot\left[1+(X_{B0}-Y)^2\right]-\left[1-(X_{B0}-Y)^2\right]^2-L^4\right\}} \tag{30}$$

$$B(Y)=\frac{\left[1-L^2-(X_{B0}-Y)^2\right]\left[\left(L^2-1\right)^3+\left(3+2L^2-5L^4\right)(X_{B0}-Y)^2+3\left(L^2-1\right)(X_{B0}-Y)^4+(X_{B0}-Y)^6\right]}{(X_{B0}-Y)^3\left\{2L^2\left[1+(X_{B0}-Y)^2\right]-\left[1-(X_{B0}-Y)^2\right]^2-L^4\right\}^2} \tag{31}$$

where $X_{B0}=x_{B0}/r$ denotes the ratio of the initial distance of the two terminals of crank inerter to the radius of crank, $L=l/r$ is the ratio of the length of connection rod to the radius of crank.

It is obtained from Eq. (29) that the non-dimensional inertial force of crank inerter can be obtained as$F_{I,n}=\frac{\mu\gamma^2}{2}\left(A(Y)Y''+B(Y)Y'^2\right)$. In$F_{I,n}$, the term $\mu\gamma^2/2$ is equal to the ratio of the inertance of a rack-and-pinion inerter which has the flywheel mass of m_0 and pinion radius of r to the isolated mass. Hence, the inertial force of the crank inerter can be seen as the modified inertial force of rack-and-pinion inerter, which can also be

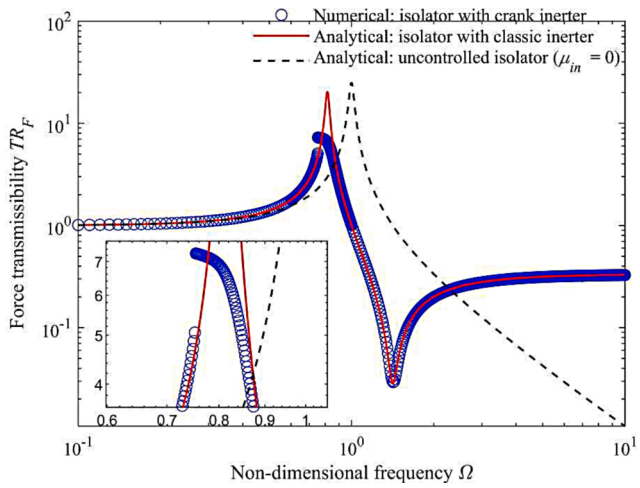

Fig. 15. Comparison of the force transmissibility for different vibration isolators with$\mu_{in} = 0.5, \xi = 0.02, F_e = 0.05$

roughly observed from the physical realization of these two inerters. For comparison, the classic rack-and-pinion inerter is employed in the isolator. The non-dimensional parameter, named the nominal inertance-to-mass ratio$\mu_{in} = \mu\gamma^2/2$, are introduced here to facilitate the corresponding comparative study. Then, by substituting the term of $\mu\gamma^2/2$ withμ_{in}, Eq. (29) can be rewritten as follows.

$$(1 + \mu_{in} \cdot A(Y))Y'' + \mu_{in} \cdot B(Y)Y'^2 + 2\xi Y' + Y = F_e \cos(\Omega\tau) \tag{32}$$

Using the fourth-order Runge-Kutta method, Eq. (32) can be solved for a certain vibration isolator with crank inerter under the harmonic force excitation. For a force excited vibration isolator, the force transmissibility is usually adopted as an index to assess the isolation performance of the isolator. The total non-dimensional force F_T transmitted to the base for the vibration isolator with crank inerter can be calculated as.

$$F_T = \mu_{in} \cdot A(X)X'' + \mu_{in} \cdot B(X)X'^2 + 2\xi X' + X \tag{33}$$

Then, the force transmissibility TR_F of the vibration isolator with crank inerter can be obtained as the ratio of the amplitude of the non-dimensional transmitted force $F_{T,a}$ to the amplitude of the non-dimensional excitation forceF_e, expressed as.

$$TR_F = \frac{F_{T,a}}{F_e} \tag{34}$$

By setting$\mu_{in} = 0.5, \xi = 0.02, L = X_{B0} = 10, F_e = 0.05$, the force transmissibility TR_F for the vibration isolator with crank inerter is numerically obtained using Eq. (34) within the range of Ω from 0.1 to 10, as shown in Fig. 15. For comparison, the analytical results of the force transmissibility for the isolator with classic inerter with $\mu_{in} = 0.5$ and the uncontrolled isolator (i.e., $\mu_{in} = 0$) are also shown in Fig. 15. The jump-up and jump-down phenomena are exhibited in the transmissibility curve of the isolator with crank inerter, which is an inherent phenomenon in the field of nonlinear vibration [43]. The corresponding non-dimensional jump-up and jump-down frequencies are obtained as 0.752 and 0.754 in the analysis case, respectively. The resonance regions of the force transmissibility curves for both the isolators with crank inerter and classic inerter are shifted to the low-frequency range compared to the uncontrolled isolators. For the isolator with crank inerter, its force transmissibility curve in the resonance region bends towards the low-frequency range, and the peak value of its force transmissibility curve is evidently lower than that for the isolator with classic inerter. In addition, it can be seen from the detailed figure that the force transmissibility curve of the isolator with crank inerter intersects to the curve of the uncontrolled isolator at the left of the intersection for the curve of the isolator with classic inerter and that of the uncontrolled isolator. This indicates that the frequency band of the isolator with crank inerter is slightly broader than that of the isolator with classic inerter relative to the uncontrolled isolator. The anti-resonances exist in force transmissibility curves for both the isolators with crank inerter and classic inerter. To sum up, based on the analysis in this section, the isolator with crank inerter is said to behave an improved performance compared to the uncontrolled isolator and the isolator with classic rack-and-pinion inerter under the same nominal inertance-to-mass ratioμ_{in}, regarding the peak force transmissibility and frequency band.

7. Conclusion

This study presents the theoretical and experimental investigation on a novel inerter element developed based on the crank mechanism, called a crank inerter. The proposed inerter device has the advantage of simple configuration and is characterized by variable negative stiffness. The constitutive model is built to simulate the mechanical behavior of the proposed crank inerter, and a parametric analysis is conducted regarding to the inertia force of the crank inerter. The test data of the prototype crank inerter and the theoretical results obtained by using the constitutive model are compared and analyzed. Effectiveness of the proposed crank inerter adopted in a vibration isolator is also investigated through dynamic analyses and comparative studies. The following conclusion can be drawn from this study about the crank inerter:

(1) The proposed crank inerter can generate apparent mass and negative stiffness effects, which can be utilized as an alternative inerter element in vibration isolation and suppression.
(2) The variable negative stiffness of the crank inerter under dynamic excitation is demonstrated by both the experimental and theoretical results. Growth of the maximum inertia force and negative stiffness is found to be more evident under a larger displacement amplitude excitation.
(3) The proposed constitutive model shows good accuracy in predicting the mechanical behavior of crank inerter in different test cases, and this gives a theoretical basis to application of the proposed crank inerter.
(4) The parametric analysis indicates that the inertia force of the crank inerter has approximately linear correlation to its terminal acceleration under a small displacement amplitude excitation. This is also verified with the test results under sinusoidal excitations with an amplitude of 5 mm. The calculation term of inertia force (Eq.) related to the relative terminal velocity of crank inerter can be ignored under a small displacement amplitude excitation (approximately $-r/3 \leqslant X \leqslant r/3$) according to experimental and theoretical results.
(5) The effect of crank inerter in an isolator is theoretically illustrated to show its improved performances of the peak force transmissibility and frequency band. This shows preliminarily the superiority of the crank inerter over the classic inerter with constant negative stiffness and inertance.

In this study, testing of the proposed crank inerter is limited to harmonic loadings. For further research, the experimental tests of the proposed crank inerter using other loading forms, such as the seismic wave and random loading, can be beneficial for verifying the

applicability of the proposed constitutive model. The analytical solutions of the dynamic responses and the experimental research for the vibration isolator with crank inerter can be performed to give a more comprehensive understanding of this system. The vibration control effect of the crank inerter should also be investigated within a structural system other than the vibration isolators. In addition, the crank inerter element can be combined with other mechanical elements (e.g., spring and damping elements) to provide superior performance. The application of the crank inerter in adaptive systems can also be considered taking into account the characteristics of variable negative stiffness of a crank inerter.

Credit authorship contribution statement

Li Zhang: Conceptualization, Methodology, Experiment, Investigation, Software, Writing – original draft, Writing – review & editing, Formal analysis, Writing – original draft. **Songtao Xue:** Methodology, Investigation, Writing – review & editing, Funding acquisition. **Ruifu Zhang:** Conceptualization, Methodology, Experiment, Investigation, Writing – original draft, Writing – review & editing, Funding acquisition. **Linfei Hao:** Experiment, Investigation, Writing – review & editing, Funding acquisition, Validation. **Chao Pan:** Methodology, Validation. **Liyu Xie:** Writing – review & editing.

Declaration of Competing Interest

The authors declare that they have no known competing financial interests or personal relationships that could have appeared to influence the work reported in this paper.

Acknowledgments

This study was supported by the National Natural Science Foundation of China (Grant No. 51978525 and 51908156), the National Key R&D Program of China (Grant No. 2021YFE0112200) and Scientific Research Fund of Institute of Engineering Mechanics, China Earthquake Administration (Grant No. 2020EEEVL0401, 2019EEVL03 and 2019D14).

References

[1] Jia YQ, Li LZ, Wang C, Lu ZD, Zhang RF. A novel shape memory alloy damping inerter for vibration mitigation. Smart Mater Struct 2019;28:115002. https://doi.org/10.1088/1361-665X/ab3dc8.
[2] Asai T, Araki Y, Ikago K. Energy harvesting potential of tuned inertial mass electromagnetic transducers. Mech Syst Signal Process 2017;84:659–72. https://doi.org/10.1016/j.ymssp.2016.07.048.
[3] Zhao ZP, Zhang RF, Jiang YY, De Domenico D, Pan C. Displacement-dependent damping inerter system for seismic response control. Appl Sci 2020;10:257. https://doi.org/10.3390/app10010257.
[4] Garrido H, Curadelli O, Ambrosini D. Improvement of tuned mass damper by using rotational inertia through tuned viscous mass damper. Eng Struct 2013;56:2149–53. https://doi.org/10.1016/j.engstruct.2013.08.044.
[5] Javidialesaadi A, Wierschem NE. An inerter-enhanced nonlinear energy sink. Mech Syst Signal Process 2019;129:449–54. https://doi.org/10.1016/j.ymssp.2019.04.047.
[6] Ikago K, Saito K, Inoue N. Seismic control of single-degree-of-freedom structure using tuned viscous mass damper. Earthq Eng Struct Dyn 2012;41:453–74. https://doi.org/10.1002/eqe.1138.
[7] Makris N, Kampas G. Seismic protection of structures with supplemental rotational inertia. J Eng Mech 2016;142(11):04016089. https://doi.org/10.1061/(ASCE)EM.1943-7889.0001152.
[8] Pan C, Zhang RF, Luo H, Li C, Shen H. Demand-based optimal design of oscillator with parallel-layout viscous inerter damper. Struct Control Health Monit 2018;25:e2051. http://doi.org/10.1002/Stc.2051.
[9] Zhao ZP, Chen QJ, Zhang RF, Jiang YY, Pan C. A negative stiffness inerter system (NSIS) for earthquake protection purposes. Smart Struct Syst 2020;26:481-93. https://doi.org/10.12989/sss.2020.26.4.481.
[10] Shi X, Zhu S. A comparative study of vibration isolation performance using negative stiffness and inerter dampers. J Franklin Inst 2019;356:7922–46. https://doi.org/10.1016/j.jfranklin.2019.02.040.
[11] Zhao ZP, Chen QJ, Zhang RF, Pan C, Jiang YY. Energy dissipation mechanism of inerter systems. Int J Mech Sci 2020;184:105845. https://doi.org/10.1016/j.ijmecsci.2020.105845.
[12] Zhang RF, Zhao ZP, Pan C, Ikago K, Xue ST. Damping enhancement principle of inerter system. Struct Control Health Monit 2020;27:e2523. https://doi.org/10.1002/stc.2523.
[13] Zhao ZP, Zhang RF, Pan C, Chen QJ, Jiang YY. Input energy reduction principle of structures with generic tuned mass damper inerter. Struct Control Health Monit 2020;28:e2644. https://doi.org/10.1002/stc.2644.
[14] Zhao ZP, Zhang RF, Jiang YY, Pan C. A tuned liquid inerter system for vibration control. Int J Mech Sci 2019;164:105171. https://doi.org/10.1016/j.ijmecsci.2019.105171.
[15] Zhang RF, Zhao ZP, Dai KS. Seismic response mitigation of a wind turbine tower using a tuned parallel inerter mass system. Eng Struct 2019;180:29–39. https://doi.org/10.1016/j.engstruct.2018.11.020.
[16] Chen QJ, Zhao ZP, Xia YY, Pan C, Luo H, Zhang RF. Comfort based floor design employing tuned inerter mass system. J Sound Vib 2019;458:143–57. https://doi.org/10.1016/j.jsv.2019.06.019.
[17] Zhang L, Xue ST, Zhang RF, Xie LY, Hao LF. Simplified multimode control of seismic response of high-rise chimneys using distributed tuned mass inerter systems (TMIS). Eng Struct 2021;228:111550. https://doi.org/10.1016/j.engstruct.2020.111550.
[18] Cao L, Li C. Tuned tandem mass dampers-inerters with broadband high effectiveness for structures under white noise base excitations. Struct Control Health Monit 2019;26(4):e2319. https://doi.org/10.1002/stc.2319.
[19] Zhao ZP, Zhang RF, Jiang YY, Pan C. Seismic response mitigation of structures with a friction pendulum inerter system. Eng Struct 2019;193:110–20. https://doi.org/10.1016/j.engstruct.2019.05.024.
[20] De Domenico D, Ricciardi G. Improving the dynamic performance of base-isolated structures via tuned mass damper and inerter devices: A comparative study. Struct Control Health Monit 2018;25:e2234. https://doi.org/10.1002/stc.2234.
[21] Ye K, Shu S, Hu L, Zhu H. Analytical solution of seismic response of base-isolated structure with supplemental inerter. Earthq Eng Struct Dyn 2019;48:1083–90. https://doi.org/10.1002/eqe.3165.
[22] Cao L, Li C. A high performance hybrid passive base-isolated system. Struct Control Health Monit 2022;29:e2887. https://doi.org/10.1002/stc.2887.
[23] Li C, Chang K, Cao L, Huang Y. Performance of a nonlinear hybrid base isolation system under the ground motions. Soil Dyn Earthq Eng 2021;143:106589. https://doi.org/10.1016/j.soildyn.2021.106589.
[24] Ma R, Bi K, Hao H. A novel rotational inertia damper for amplifying fluid resistance: Experiment and mechanical model. Mech Syst Signal Process 2021;149:107313. https://doi.org/10.1016/j.ymssp.2020.107313.
[25] Nakamura Y, Fukukita A, Tamura K, Yamazaki I, Matsuoka T, Hiramoto K et al. Seismic response control using electromagnetic inertial mass dampers. Earthq Eng Struct Dyn 2014;43:507-27. https://doi.org/ 10.1002/eqe.2355.
[26] Sugiura K, Watanabe Y, Asai T, Araki Y, Ikago K. Experimental characterization and performance improvement evaluation of an electromagnetic transducer utilizing a tuned inerter. J Vib Control 2020;26:56–72. https://doi.org/10.1177/1077546319876396.
[27] Zhang RF, Zhao ZP, Lin XC, Zhang LX. Optimal design of inerter systems for the force-transmission suppression of oscillating structures. Earthq Eng Eng Vib 2022;21(2):441–54. https://doi.org/10.1007/s11803-022-2090-7.
[28] Kawamata S. Development of a vibration control system of structures by means of mass pumps. Tokyo, Japan: Institute of Ind Sci Univer Tokyo; 1973.
[29] Kawamata S, Funaki N, Itoh Y. Passive control of building frames by means of liquid dampers sealed by viscoelastic material. In: 12th World Conference on Earthquake Engineering. Auckland, New Zealand, 2000.
[30] Saito K, Toyota K, Nagae K, Sugimura Y, Nakano T, Nakaminam IS et al. Dynamic loading test and its application to a high-rase building of viscous damping devices with amplification system. In: Proceedings of the Third World Conference on Structural Control. Como, Italy, 2002.
[31] Saito K, Sugimura Y, Nakaminami S, Kida H, Inoue N. Vibration tests of 1-story response control system using inertial mass and optimized soft spring and viscous element. In: Proceedings of the 14th World Conference on Earthquake Engineering. Beijing, China, 2008.
[32] Ikago K, Sugimura Y, Saito K, Inoue N. Optimum seismic response control of multiple degree of freedom structures using tuned viscous mass dampers. In: Proceedings of the Tenth International Conference on Computational Structures Technology. Stirlingshire, Scotland, 2010.
[33] Wang FC, Hong MF, Lin TC. Designing and testing a hydraulic inerter. Proc Inst Mech Eng Part C-J Mech Eng Sci 2011;225:66–72. https://doi.org/10.1243/09544062JMES2199.

[34] John EDA, Wagg DJ. Design and testing of a frictionless mechanical inerter device using living-hinges. J Franklin Inst 2019;356:7650–68. https://doi.org/10.1016/j.jfranklin.2019.01.036.
[35] Yuan S, Sun Y, Wang M, Ding J, Zhao J, Huang Y et al. Tunable negative stiffness spring using maxwell normal stress. Int J Mech Sci 2021;193:106127. https://doi.org/10.1016/j.ijmecsci.2020.106127.
[36] Pu H, Yuan S, Peng Y, Meng K, Zhao J, Xie R, et al. Multi-layer electromagnetic spring with tunable negative stiffness for semi-active vibration isolation. Mech Syst Signal Process 2019;121:942–60.
[37] Lazarek M, Brzeski P, Perlikowski P. Design and modeling of the CVT for adjustable inerter. J Franklin Inst 2019;356:7611–25. https://doi.org/10.1016/j.jfranklin.2018.11.011.
[38] Faraj R, Jankowski L, Graczykowski C, Holnicki-Szulc J. Can the inerter be a successful shock-absorber? The case of a ball-screw inerter with a variable thread lead. J Franklin Inst 2019;356:7855–72. https://doi.org/10.1016/j.jfranklin.2019.04.012.
[39] Moraes FH, Silveira M, Paupitz Goncalves PJ. On the dynamics of a vibration isolator with geometrically nonlinear inerter. Nonlinear Dyn 2018;93:1325–40. https://doi.org/10.1007/s11071-018-4262-6.
[40] Wang Y, Li HX, Cheng C, Ding H, Chen LQ. A nonlinear stiffness and nonlinear inertial vibration isolator. J Vib Control 2020;27:1336–52. https://doi.org/10.1177/1077546320940924.
[41] Mirza Hessabi R, Mercan O. Investigations of the application of gyro-mass dampers with various types of supplemental dampers for vibration control of building structures. Eng Struct 2016;126:174–86. https://doi.org/10.1016/j.engstruct.2016.07.045.
[42] Wang FC, Su WJ. Impact of inerter nonlinearities on vehicle suspension control. Veh Syst Dyn 2008;46(7):575–95. https://doi.org/10.1080/00423110701519031.
[43] Nayfeh AH, Mook DT. Nonlinear oscillations. New York: John Wiley & Sons; 2008.